Development of a Co–deposition method for Deposition of Low–Contamination Pyrite Thin Films

by

Aditya Walimbe

A Thesis Presented in Partial Fulfillment
of the Requirements for the Degree
Master of Science

Approved April 2016 by the
Graduate Supervisory Committee:

Nathan Newman, Chair
Rakesh Singh
Terry Alford

ARIZONA STATE UNIVERSITY

May 2016

ABSTRACT

Pyrite is a 0.95 eV bandgap semiconductor which is purported to have great potential in widespread, low–cost photovoltaic cells. A thorough material selection process was used in the design of a pyrite sequential vapor deposition chamber aimed at reducing and possibly eliminating contamination during thin film growth. The design process focused on identifying materials that do not produce volatile components when exposed to high temperatures and high sulfur pressures. Once the materials were identified and design was completed, the ultra–high vacuum growth system was constructed and tested.

Pyrite thin films were deposited using the upgraded sequential vapor deposition chamber by varying the substrate temperature from 250°C to 420°C during deposition, keeping sulfur pressure constant at 1 Torr. Secondary Ion Mass Spectrometry (SIMS) results showed that all contaminants in the films were reduced in concentration by orders of magnitude from those grown with the previous system. Characterization techniques of Rutherford Back–scattering Spectrometry (RBS), X–Ray Diffraction (XRD), Raman Spectroscopy, Optical Profilometry and UV/Vis/Near–IR Spectroscopy were performed on the deposited thin films. The results indicate that stoichiometric ratio of S:Fe, structural–quality (epitaxy), optical roughness and percentage of pyrite in the deposited thin films improve with increase in deposition temperature. A Tauc plot of the optical measurements indicates that the pyrite thin films have a bandgap of 0.94 eV.

ACKNOWLEDGMENTS

I express my gratitude towards Prof. Nathan Newman, my research advisor, for providing me the opportunity to undertake this project and his continuous guidance throughout the project. I appreciate the motivation and encouragement he provided to help me perform some challenging experiments in this project. I extend my thanks to Dr. Rakesh Singh for his guidance and important discussions regarding results from Rutherford Back-Scattering Spectrometry and for agreeing to serve on my Supervisory Committee. I am grateful to Prof. Terry Alford for accepting to serve on my Supervisory Committee. I would like to make a special mention of the help extended by Mr. Cameron Kopas and Mr. John Domenico for XRD characterization, Mr. Cougar Garcia and Mr. Matthew Edwards for RBS tool, simulation and analysis of the data, Mr. Aditya Ravi and Mr. Siddhesh Gajare for helping me with electrical measurements and assembly of certain parts of chamber itself. I am also grateful to Mr. Shengke Zhang and Mr. Makram Abd El Qader for motivating me over the duration of my project. I thank Mr. Thomas Chamberlin for his extensive support with SolidWorks in designing components of the chamber. I thank Mr. James Makar from ASU machine shop for fabricating some vital parts of my chamber. I am particularly grateful to Mr. Richard Henley for his continuous support in fixing equipments and also procuring supplies required for the chamber. The use of facilities in the LeRoy Eyring Center for Solid State Science at Arizona State University is acknowledged. Last but not least, I would like to convey thanks to all other members of Newman Research group for their constant support in carrying out this project.

TABLE OF CONTENTS

Page

LIST OF TABLES

Table Page

LIST OF FIGURES

Figure Page

Figure Page

CHAPTER 1

INTRODUCTION

1.1 Operation and efficiency of single–cell photovoltaic cell

A p–n junction photovoltaic (PV) cell operates by absorbing a photon of light with energy greater than or equal to bandgap of its material. The electrons and holes that are generated drift to the edge of the depletion region and then through the semiconductor neutral region and then, are collected at their respective electrodes. The efficiency of a PV cell primarily depends on: (i) fraction of light with energies above the bandgap, (ii) energy lost to thermalization of photons above the bandgap and (iii) the ratio between the time charge carriers take to cross the depletion region and their lifetimes. According to Shockley and Queisser [1], recombination between electrons and holes resulting in radiation, i.e. radiative recombination, determines the detailed balance limit for efficiency by setting a limit to minority carrier lifetimes. This theoretical limit of efficiency, also called Shockley–Queisser limit, has maximum value of 30% at 1.1 eV bandgap exposed to sunlight of 1.5 global air mass, as shown in Fig. 1.

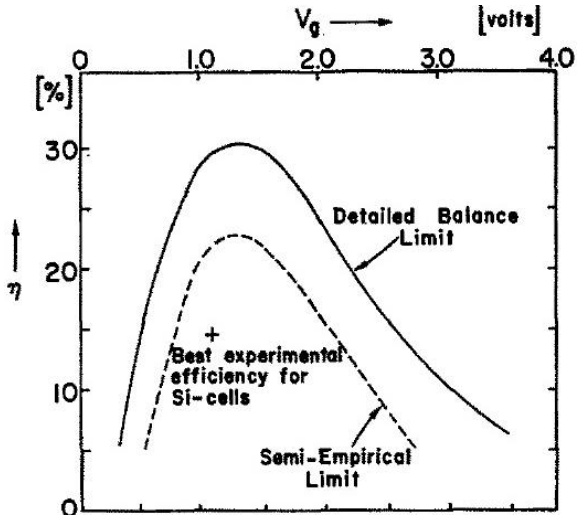

Fig. 1. Plot showing dependence of efficiency of single–junction solar cell on bandgap [1]

From the data published by Green, M. A. et al. (2015) [2], crystalline silicon (x–Si) photovoltaic cells have obtained an efficiency of up to 25.6% ± 0.5%, when measured at 25°C in a global AM 1.5 spectrum (1000W/m^2). On the other hand, low–cost photovoltaic technologies such as amorphous silicon (a–Si) and micro–crystalline silicon have exhibited efficiencies as high as 10.2% ± 0.3% and 11.4% ± 0.3%, respectively. Thin film cells based on gallium arsenide (GaAs), chalcogenides such as copper indium gallium selenide ($CuIn_xGa_{1-x}Se_2$; CIGS) and cadmium telluride (CdTe) respectively show cell efficiency of 28.8% ± 0.9%, 20.5% ± 0.6% and 21.0% ± 0.4% [2]. Due to its low absorption cross–section and high processing cost, x–Si does not show promise for a low–cost, thin film PV device. However, toxicity, scarcity and thereby the cost associated using As, In, Ga and Cd in the GaAs, CIGS and CdTe cells limits their potential for wide–spread use in the future. Thus, when seeking alternatives for present PV materials, these drawbacks along with the need of decrease in cost, must be given prime importance.

Semiconductors like copper zinc tin sulfide (Cu_2ZnSnS_4; CZTS), pyrite (FeS_2) and copper oxide (CuO) have been identified as materials which could potentially overcome the drawbacks of conventional PV materials and attain wide–spread use by the PV industry in the future [3]. Each of these semiconductors are comprised on inexpensive materials and have: (a) an appropriate bandgap for efficient conversion, (b) low toxicity, (c) low extraction cost, and (d) a high absorption cross–section [4].

1.2 Pyrite as a candidate for thin film photovoltaic cells

Fig. 2 shows the binary phase diagram of iron and sulfur. As noted in Table 1, there are several iron sulfides with different iron (Fe) and sulfur (S) stoichiometric ratios,

different crystal structures and thus, different properties. This has proven to make the synthesis of a phase–pure, high–quality pyrite thin film challenging.

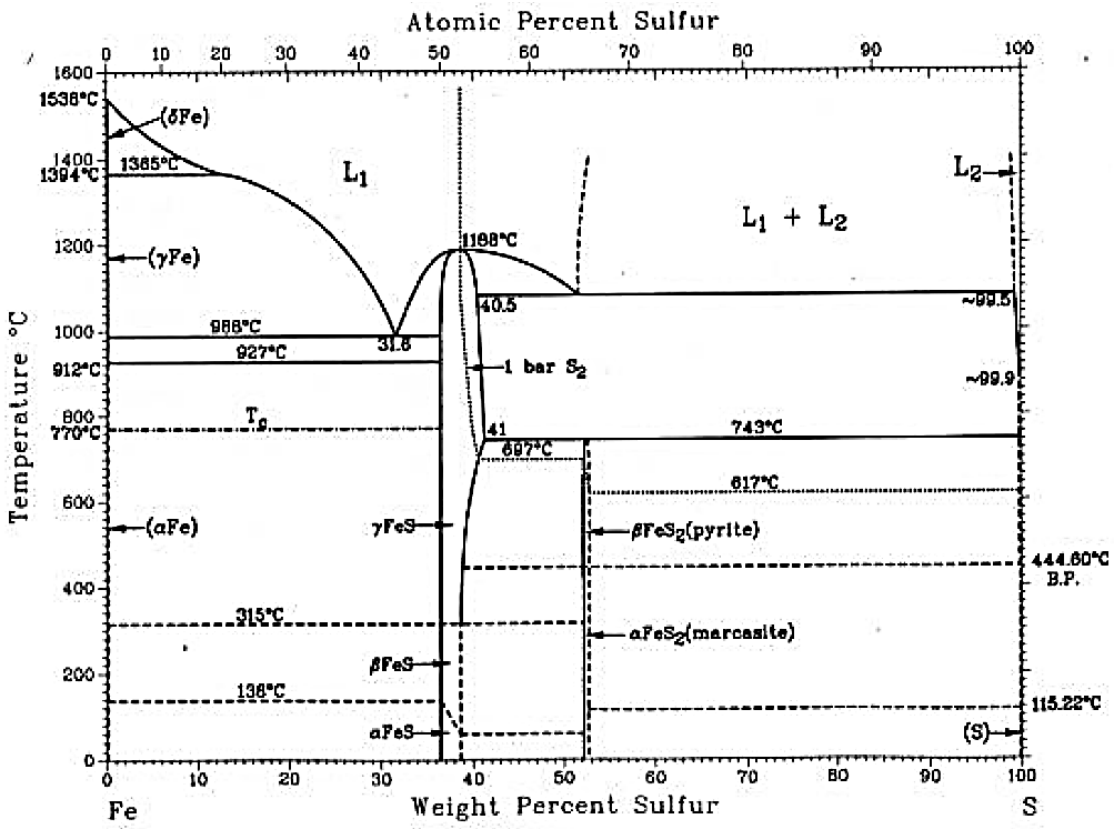

Fig. 2. Iron – Sulfur binary phase diagram [5]

Table 1. Sulfides present in iron–sulfur phase diagram [5]

Phase	**Composition, wt. % S**	**Crystal structure**
γFeS	36.5 to 41	*
Troilite; βFeS	36.5 to ~38	Hexagonal
αFeS	36.5 to ~38	*
Pyrite; βFeS_2	~53.5	Cubic
Marcasite; αFeS_2	~53.5	Orthorhombic

* Crystal structure can be hexagonal or monoclinic.

1.3 Deposition of pyrite thin films

Experimental techniques used to grow pyrite thin films include chemical vapor transport (CVT), metal–organic chemical vapor deposition (MOCVD), spray pyrolysis methods and sulfurization of iron and iron oxides [4]. These methods extensively rely on the use of chemical compound precursors which can be expensive and toxic.

A high vapor pressure of sulfur is required when using physical vapor deposition (PVD) techniques to synthesize pyrite. Vahidi M. et al. (2013) developed a simple and robust PVD layer–by–layer growth process to make high–quality, single phase pyrite thin films from their elemental constituents, S and Fe [6]. This technique was subsequently modified by Wertheim A. to achieve better control of sulfur pressure and substrate temperature. This is the sequential vapor deposition system in which heated substrates are alternately exposed to iron in high vacuum and sulfur at high pressure (0.1 Torr – 1 Torr) using a rotating substrate holder mechanism as seen in fig. 3.

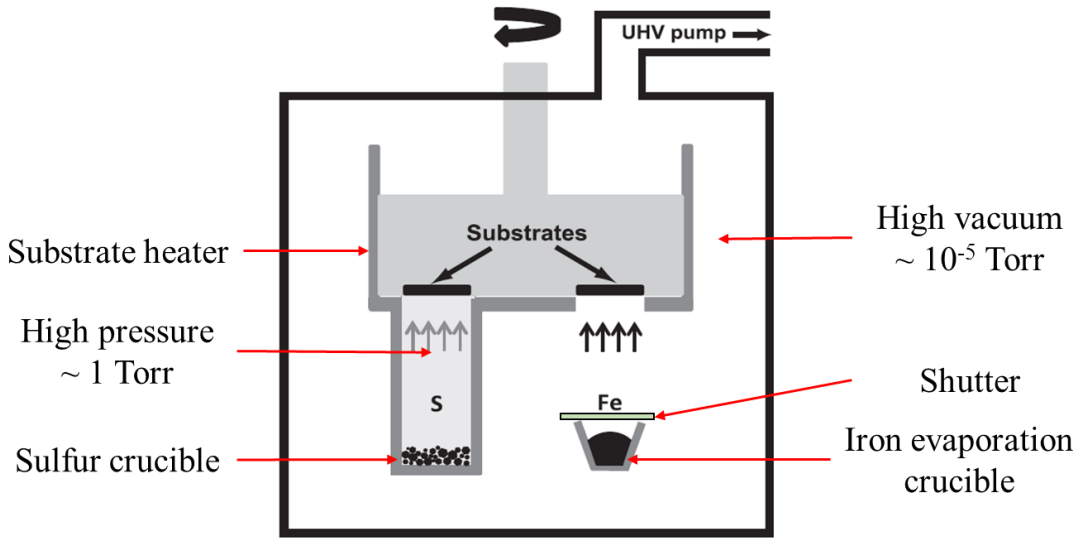

Fig. 3. Schematic diagram of sequential evaporation system [6]

The films deposited in this system were found to have a significant level of contamination in the thin films arising from re–evaporation of the reaction products between sulfur and chamber components (eg. gaskets, substrate heater and electrical feedthroughs). My work focused on reducing the concentration of contaminants and improving the quality of deposited thin films. I have followed a similar deposition process, however, growths were performed at higher sulfur pressure, i.e. 1 Torr. The following chapters elaborate on the motivation for this project, the procedures followed when conducting experiments, results of characterization techniques and conclusions based on these results.

CHAPTER 2

MOTIVATION

In a study conducted by Wadia C. et al. (2009) [3], the potential to produce inexpensive and efficient photovoltaics for widespread use was evaluate for 23 inorganic semiconductors. The investigators took into account the single junction efficiency limits, cost of extraction of respective raw materials, worldwide material reserves and the electricity production potential.

Iron pyrite (FeS_2), crystalline silicon (x–Si), amorphous silicon (a–Si) and gallium arsenide have raw material cost of \$1.9 x 10^{-8}, \$3.9 x 10^{-4}, \$1.8 x 10^{-6} and \$2.5 x 10^{-3} for every watt (\$/W) of the potential amount of electricity produced by photovoltaic cells made from these materials. About 55% of total installed cost for existing PV comes from the module cost. If pyrite–based photovoltaic cells could be produced with inexpensive methods and also achieve the same performance as x–Si, it could produce 10^2 to 10^3 times the current global annual electricity consumption compared to 10^{-2} to 10^{-1} times achievable by x–Si [3].

In chapter 1, I discussed fundamental aspects of operation, cell efficiency and material choice for a photovoltaic cell. Large bandgap materials (> ~1.3 eV) absorb a relatively small part of the available spectrum, thereby exhibiting smaller short–circuit current (I_{SC}), while small bandgap materials absorb broad section of the spectrum, but exhibit a lower open–circuit voltage (V_{OC}). Poor quality semiconductors with significant concentrations of midgap levels have low carrier mobilities and minority–carrier lifetimes, also resulting in poor cell efficiencies. Such performance degrading levels are formed by

native and impurity defects. Although the sequential evaporation process developed by my group showed great promise to make stoichiometric, high–structural quality pyrite thin films, methods to prevent high level of contamination during deposition had not been developed. The primary objective of my project was reduction and elimination of contaminants in deposited pyrite thin films.

CHAPTER 3

EXPERIMENTAL PROCEDURE

In this chapter, the procedures used to carry out the experiments in this project are outlined. The first section, 3.1, describes the design, fabrication and testing of the new upgraded growth system. In the second section, 3.2, procedures for depositing pyrite thin films are elaborated. Finally, in section 3.3, the capabilities and methodology of characterization techniques has been reviewed.

3.1 Design of substrate holder for upgraded chamber

The secondary ion mass spectrometry (SIMS) analysis performed on thin films deposited using sequential vapor deposition chamber designed by Vahidi M. et al. [6] indicated large concentrations of impurities such as copper (Cu), chromium (Cr), nickel (Ni) and manganese (Mn). The copper impurity arose from re–evaporation of products of reaction of sulfur with components of vacuum chamber, mainly, gaskets used for vacuum-sealing flanges and electrical feedthroughs used to supply power to the heating elements. The source of tungsten impurity was identified to be the iron–evaporation crucible. The source for Ni, Cr and other constituents was the heated stainless steel substrate holder, bottom–plate and bottom–disc. These components were exposed to high sulfur pressures and temperatures (300°C – 450°C), which resulted in a strong reaction with sulfur. To eliminate contamination, it is necessary to eliminate materials which react with sulfur and form volatile products. Fig. 4 shows a schematic of the deposition chamber indicating main components of the system.

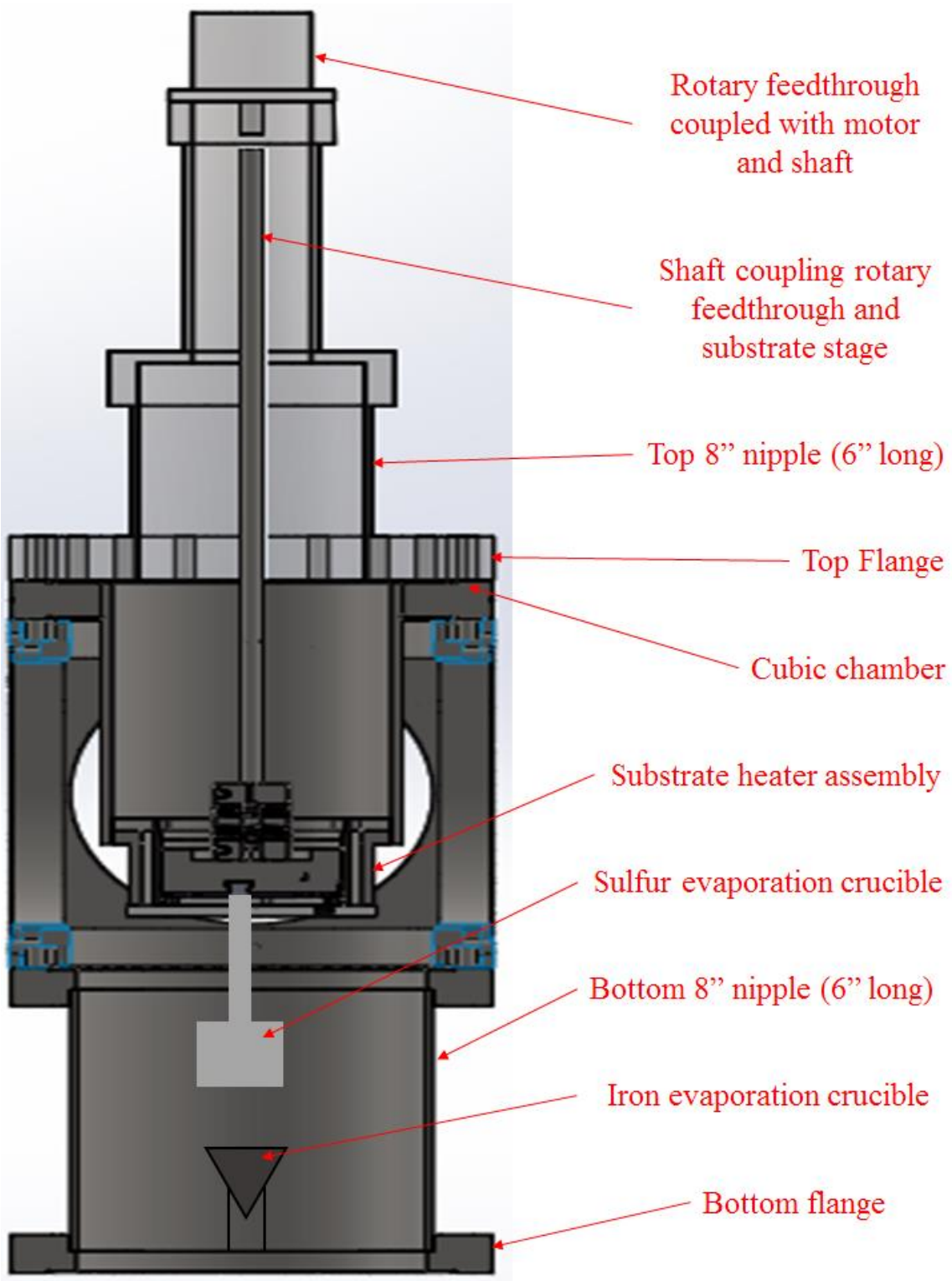

Fig. 4. Design of the chamber used of pyrite thin film deposition showing important parts

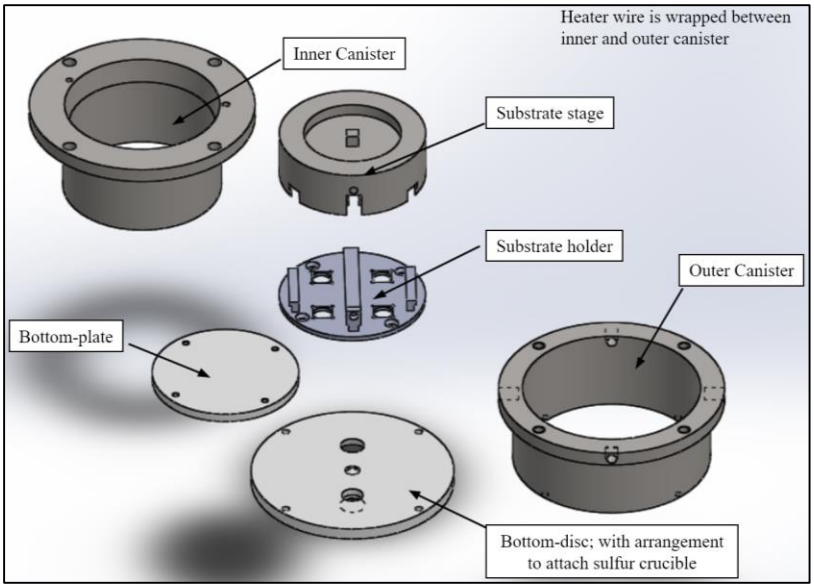

Fig. 5. Design images of the substrate heater assembly used in the upgraded chamber

Some common metals, compounds and ceramics commonly used in vacuum systems were chosen for investigation. For each candidate material, potential reaction products formed when exposed to sulfur under the temperature and pressure conditions present in chamber were determined using appropriate phase diagrams, including those presented as Ellingham diagrams (fig. 6). To carry out this experiment, the amount of sulfur required to attain a pressure of 100 Torr in the ampoule was determined. Then a specimen of each candidate material was weighed, placed in a separate ampoule with appropriate amount of sulfur and then vacuum–sealed. To test the materials under accelerated degradation conditions, the ampoules were subsequently heated in a tubular furnace at temperature to 450°C for 24 hours. After the heat treatment, each of the materials was removed from the ampoules and characterized using X-Ray Diffraction (XRD) for phase identification, Rutherford Back-scattering Spectrometry (RBS) for determination of the thickness and composition of the reacted layer and Thermo-gravimetric Analysis (TGA) for quantifying the volatility of the reaction products.

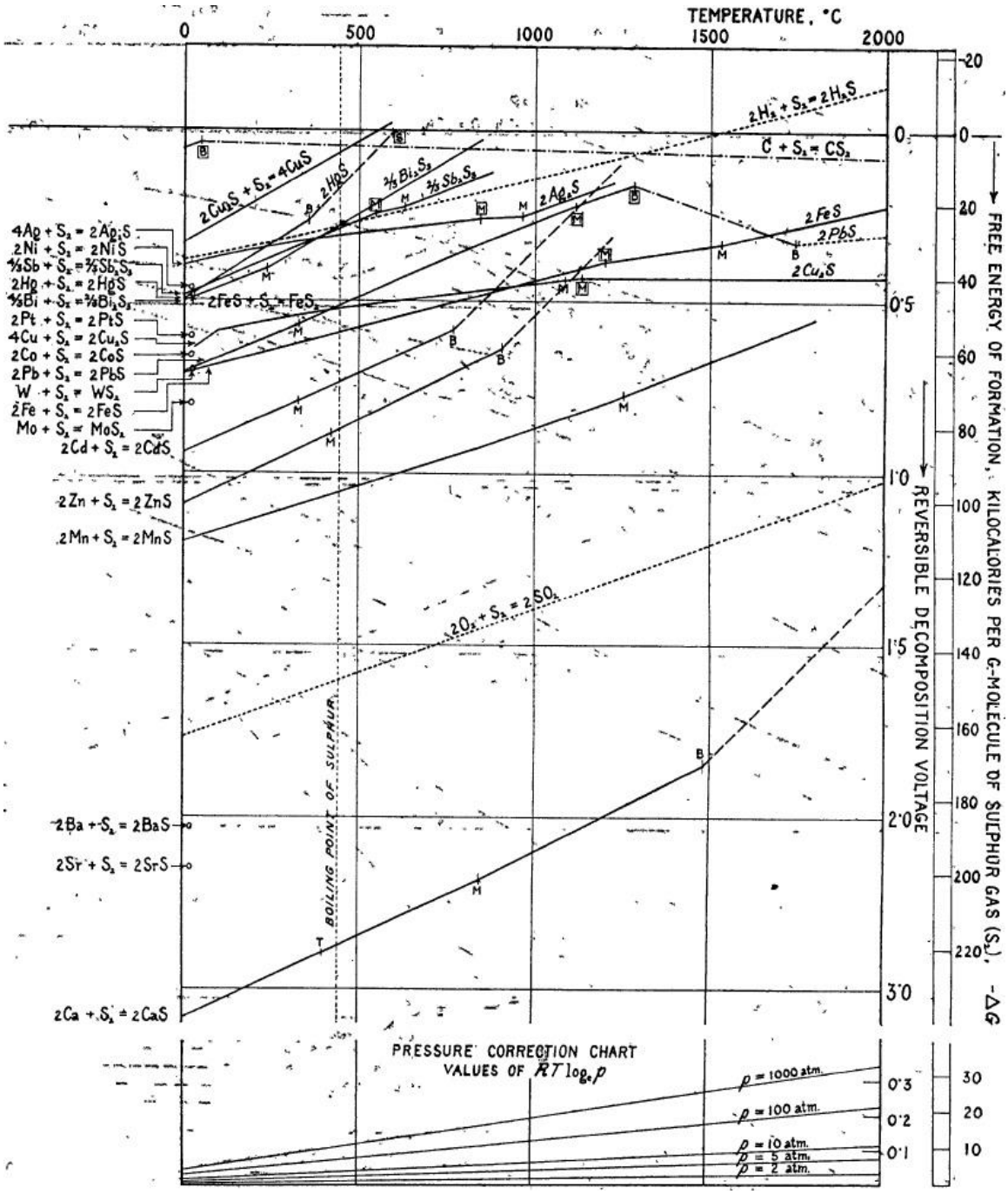

Fig. 6. Ellingham diagram of known sulfides [8]

3.2 Deposition of pyrite thin films

The substrate holder for deposition of pyrite thin films was designed to hold 4 substrates of dimensions 1 cm x 1 cm x 500 μm. I typically used following substrates: 1 x

Si (100), 2 x SiO_2–coated Si and 1 x Al_2O_3 (r–plane) for the following reasons. Iron pyrite (FeS_2) and silicon (Si) both have a cubic structure and the lattice mismatch is only 0.25% (FeS_2: 5.418 Å; Si 5.431 Å). The SiO_2–coated Si substrates have an amorphous and insulating thermal–oxide buffer layer of approximately 2000 Å. Prior to loading substrates in the chamber, the surfaces were cleaned by ultra–sonicating them in semiconductor–grade acetone followed by isopropyl alcohol for 5 minutes. All substrates, except Si (100), were rinsed with de–ionized (DI) water which was subsequently blown off with dry N_2 gas and then mounted onto the substrate holder. Silicon substrates were subjected to an additional etch step in order to remove the native oxide layer from its surface. The Si substrate surface was exposed for 3 minutes to a freshly prepared 5% (by volume) solution of HF acid in DI water, followed by rinsing with DI water and blow–off with dry N_2. Immediately after this step, the Si substrate was mounted on the substrate holder, which was subsequently loaded into the chamber and connected with the substrate heater assembly. The chamber was then pumped down to high vacuum conditions and typically left overnight to achieve a low base pressure (typically on the order of 1.2×10^{-5} Torr).

For conducting each deposition experiment, a single–step temperature sequence for substrate heater was used. The raw materials used for deposition experiments were iron (Alfa Aesar; 99.98% metals basis purity) and sulfur (STREM Chemicals; 99.999% purity) loaded into their respective crucibles. Iron was evaporated from an alumina–coated tungsten crucible heated by passing constant current (37.5 A) through it. The sulfur pressure was maintained at either 100 mTorr or 1 Torr by heating sulfur–evaporation crucible to corresponding temperature of 147°C or 180°C. Through the course of the experiment, substrate holder along with substrate stage assembly was rotated inside the

substrate heater at rotation speed of ~5 rpm. The substrate temperature chosen for each deposition was varied between 250°C and 425°C (in steps of 25°C). Substrates were heated from room temperature to the deposition temperature, held at that temperature in presence of iron–evaporation and sulfur at 1 Torr for growth duration (90 minutes), annealed at same temperature for 30 minutes and then cooled to room temperature in vacuum. When the substrates reached the deposition temperature and the sulfur crucible temperature was stable at 147°C or 180°C, the iron–evaporation crucible was heated up to temperature in ~1 minute and its shutter was opened. After 90 minutes, the shutter was closed and the current supplied to the iron–evaporation crucible was brought down to zero over a period of 2 minutes. During annealing, the substrate temperature and 1 Torr sulfur pressure were maintained at same values as during deposition. At the end of annealing stage, the current supplied to the substrate heater as well as the sulfur–evaporation crucible was stopped and the substrates were allowed to cool to room temperature. After each deposition, the substrates with their deposited thin films were removed from the chamber for characterization.

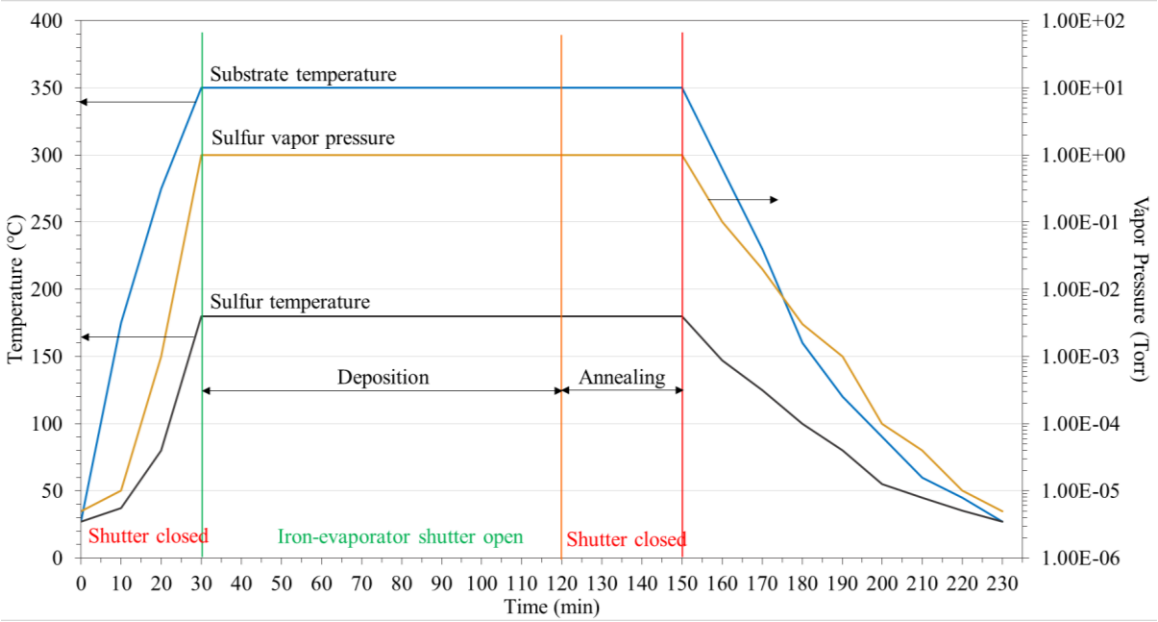

Fig. 7. Plot showing profile of process parameters for deposition at 350°C and 1 Torr

3.3 Characterization of deposited thin films

Rutherford Back-scattering Spectrometry (RBS) was performed to qualitatively determine the composition, stoichiometry and thickness of the deposited thin films. RBS was performed under non–resonance, as well as at oxygen resonance, conditions to improve the sensitivity of detecting oxygen incorporation in the films. Quantitative analysis of these measurements was carried out using RUMP software simulations.

Due to limited resolution of RBS and relatively close atomic weights of iron and contaminant metals identified earlier, Helium Induced X–ray Emission was also performed to determine the impurity content.

Secondary Ion Mass Spectrometry (SIMS) was used to determine level of contamination in the deposited films. SIMS was only performed on few films to study trace levels of contamination.

Glancing–angle X–ray Diffraction (GA–XRD) was performed on thin films deposited on Si (100) substrates to determine the crystal quality of the primary phase and the detection of any secondary phases of iron disulfide. Marcasite is a phase in iron-sulfur phase diagram that has chemical composition FeS_2 and although it has orthorhombic crystal structure, peaks in the XRD pattern from both marcasite and pyrite occur at similar values of 2θ. Raman Spectroscopy was also used to distinguish between pyrite and marcasite as Raman shift occurs at distinct wavelengths for each of these phases.

Measurements were performed using an optical profilometer to investigate the surface topography characteristics. Along with these, transmission and reflection measurements were also performed in UV/Vis/Near–IR range of spectrum to measure the absorption and absorbance of pyrite thin films with the aim of determining the bandgap of iron pyrite and detecting any mid–gap levels that may be present.

CHAPTER 4

RESULTS AND DISCUSSIONS

4.1 Selection of material for substrate holder

As discussed earlier in section 3.1, a study was conducted to evaluate the potential use in the fabrication of substrate holder, bottom–plate and bottom–disc in the upgraded chamber. A list of the materials studied along with the enthalpy of formation of their respective sulfides is presented in Table 2. Visual examination of the materials after heating in sulfur environment led to elimination of copper and silver due to severe corrosion. The thickness of reacted layer and products of reaction were determined using RBS for the other materials. Based on these results, the potential materials for building substrate heater were identified to be: aluminum, alumina, Macor, Si and SiO_2–coated stainless steel. Considering the constant physical contact between the bottom–plate and bottom–disc during substrate stage rotation, SiO_2–coated stainless steel was ruled out. The intricate shape of components, brittle nature and high cost of manufacturing make Si and alumina a poor choice of material for this purpose. RBS results for the aluminum sample indicated a strong surface reaction, which is expected, given the high enthalpy of formation of Al_2S_3 (-724 kJ/mol). A careful investigation of the Al–S, Al–Fe and Macor–related phase diagram indicates that no volatile products will form at least up to temperature of 530°C. To experimentally measure the volatility of products on the samples after the sulfur–environment heat–treatment, thermo–gravimetric analysis (TGA) was performed. The observed initial gain in mass for all samples is due to buoyancy effect in the instrument.

Both Macor and aluminum showed a loss of mass at ~ 145°C (sulfur vapor pressure ~ 100 mTorr).

Table 2. Enthalpy of formation for sulfides of materials chosen for the study

Material	**Sulfide**	**Enthalpy of formation (kJ/mol)**
Aluminum (Al)	Al_2S_3	-724
	AlS	N/A
Alumina (Al_2O_3)	Same as above	
Macor *	–	
Silver (Ag)	Ag_2S	-32.59
Copper (Cu)	CuS	-53.10
Silicon (Si)	SiS_2	-254.60
SiO_2–coated SS	Same as above	
* Macor is a machinable glass–ceramic with a rough composition of: 55% fluorophlogopite mica and 45% borosilicate glass [Courtesy: Corning Inc.]		

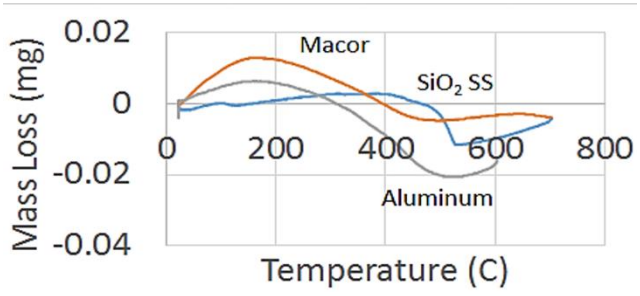

Fig. 8. Results of TGA for Al, Macor and SiO_2–coated stainless steel samples

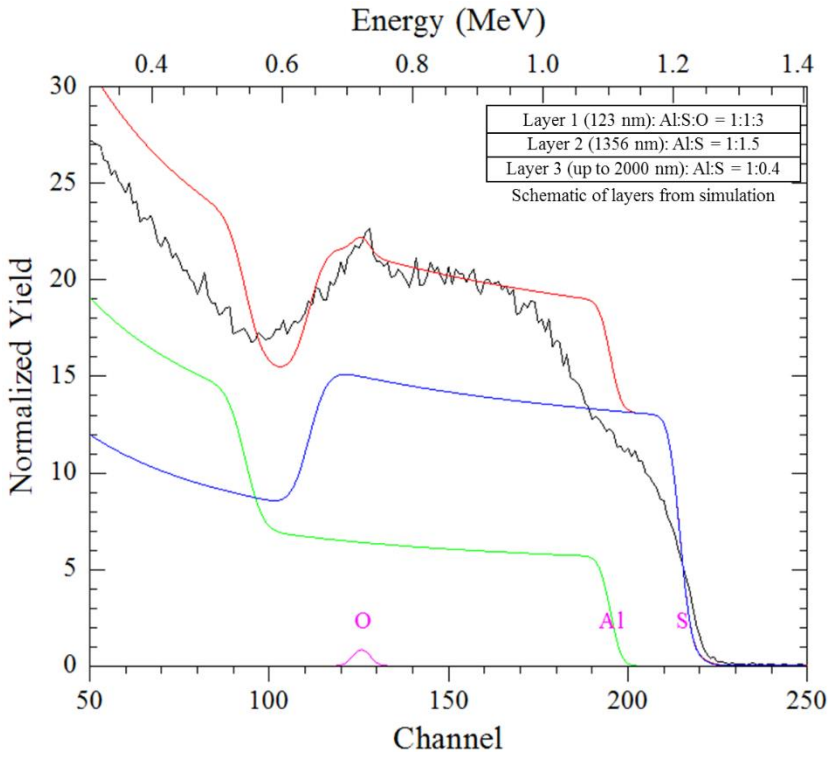

Fig. 9. RBS plot for Al sample showing reaction products and layer thicknesses

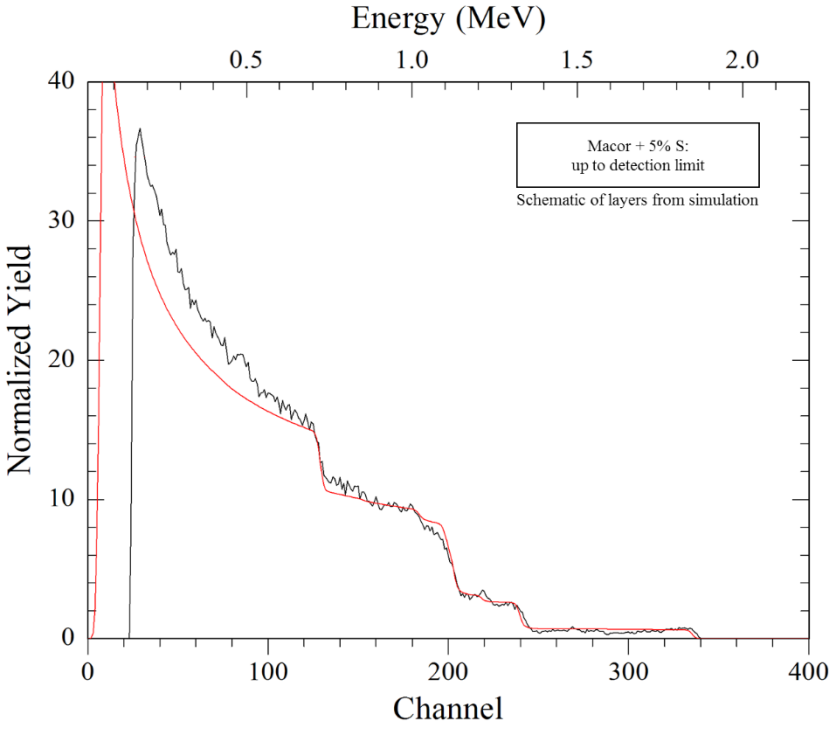

Fig. 10. RBS plot for Macor sample showing no reaction with sulfur

4.2 Helium Induced X–ray Emission (HeIXE)

Aluminum was used to fabricate the substrate holder and bottom–disc of the heater assembly. Since the substrate holder surrounds and is also in direct physical contact with the substrates for the entire duration of the growth, it is essential to check if aluminum contaminates the deposited films in the upgraded chamber system. As mentioned in section 3.2, the pyrite thin films were deposited on silicon, thermally–oxidized silicon and sapphire substrates.

HeIXE was performed on a thin film deposited (PTF073015) on magnesium oxide (MgO) substrate. There was no detectable aluminum contamination in the deposited thin films up to the detection limit of ~100 ppm as shown in the next figure.

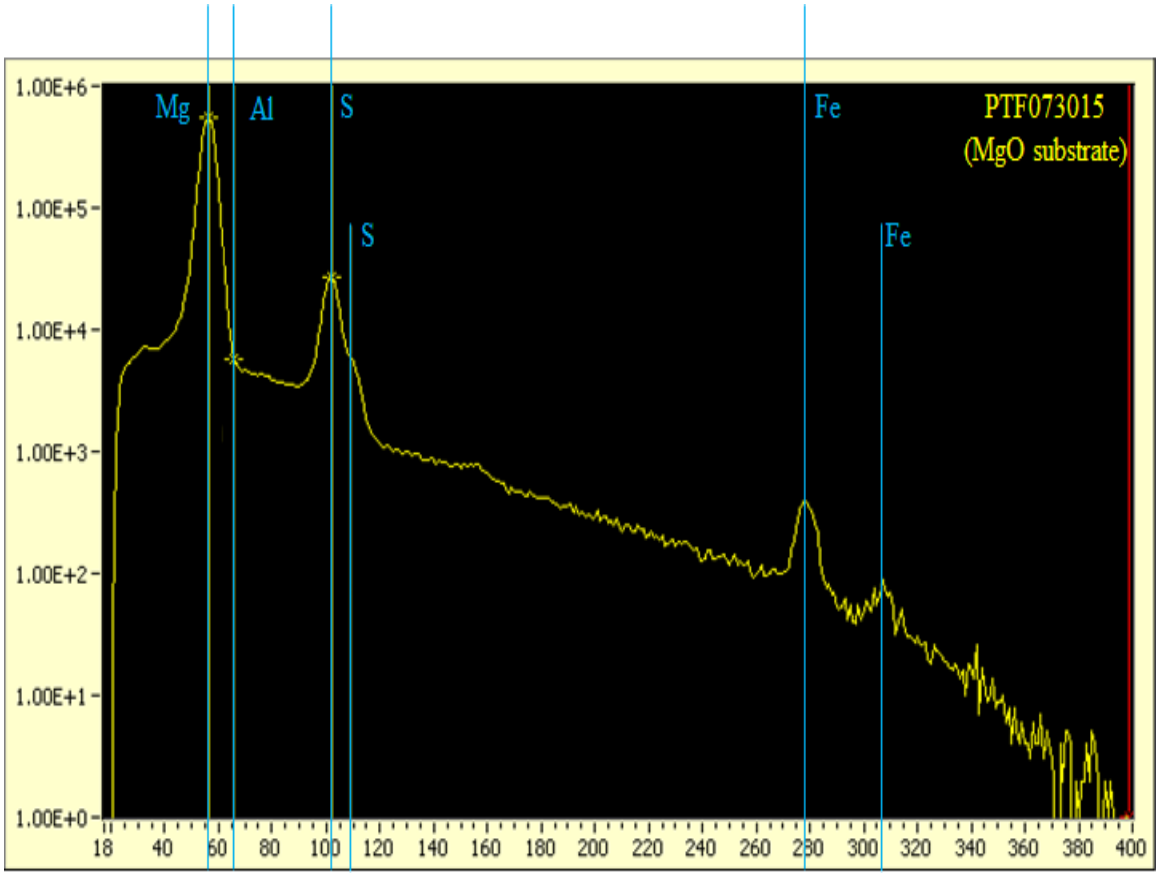

Fig. 11. HeIXE plot showing no aluminum contamination of deposited thin film

4.3 Secondary Ion Mass Spectrometry (SIMS)

Other contaminants such as copper (Cu), nickel (Ni), chromium (Cr) could not be detected and quantified by HeIXE due to the limited sensitivity of this technique. To measure the concentration of these contaminants, secondary ion mass spectrometry (SIMS) was performed on 2 representative thin films. Table 3 compares the SIMS results collected from deposited thin films in both chamber systems. The contamination level of aluminum in films deposited in the upgraded chamber is 1.2 ppm and 9.5 ppm, well below the HeIXE detection limit. The concentration of all the elemental contaminants has been reduced by at least 2 orders of magnitude for films deposited in this upgraded system with the Al substrate holder, over that from the old system with the stainless steel substrate holder.

Table 3. Summary of SIMS performed on deposited thin films

Impurity Element	**Impurity concentration (ppm)**			
	Old Chamber		**Upgraded chamber**	
	PD060814	**PD061114**	**PTF102915**	**PTF111615**
Magnesium	1027	901	2.81	8.27
Aluminum	No data	No data	1.20	9.52
Chlorine	297	1216	14.31	0.00
Calcium	217	100	0.61	16.22
Titanium	361	201	0.13	2.95
Chromium	188	223	2.03	5.64
Manganese	311	264	1.15	11.01
Nickel	694	2404	123.14	220.03
Copper	2059	2462	2.80	1.19
Zinc	1244	5064	30.20	42.41
Bromine	7237	1094	0.00	0.00
Molybdenum	13	16	0.00	0.00
Tungsten	4	33	0.14	2.00
Lead	270	335	0.00	0.00

In order to eliminate contamination from copper, I replaced all copper gaskets with alternate materials. Aluminum gaskets were used in all cases, except for one Viton gasket between the top–nipple and substrate–heater housing assembly (refer to fig. 4). Viton was used in this case to save time when repairs were needed inside the chamber, an event that occurred relatively frequently during the initial stages of this project. Finally, I replaced all copper electrical feedthroughs with those made from iron. In this way, the use of copper in the chamber was completely eliminated.

Lead was another contaminant found in films made with the first generation heater. This was found to come from a lubricant used on the rotating substrate stage. This lubricant was not needed or used in my design because of the more precise alignment tolerances between the substrate stage and polished bottom–disc. I found that the ever–present sulfur can work as a very effective lubricant itself.

Alumina–coated tungsten crucibles were used to evaporate iron. Although both chambers used crucibles of the same shape (fig. 8), in the old chamber, it was made by bending legs of a commercially available crucible design. Such bending resulting in cracking and flaking of alumina, thereby exposing the tungsten wire. We were able to reduce the tungsten impurity concentration in the deposited films by using "custom–made" crucibles that had their legs bent first and then followed by the application of the alumina coating [Courtesy: R. D. Mathis Company].

The source of chromium (Cr) and nickel (Ni) contamination was attributed to the substrate holder's stainless steel being exposed to high temperatures in the sulfur growth environment. Evidence of etching could be seen throughout the heater assembly, especially in a circular erosion track in the bottom–plate near the substrate mounts in the old chamber.

By replacing these components with aluminum ones, the concentration of chromium (Cr), nickel (Ni), manganese (Mn), zinc (Zn) and titanium (Ti) is markedly diminished in the deposited thin films. Contamination from Ni, though lower than previous chamber, was still found to be considerable (120 ppm and 220 ppm in the two films). This contamination arises from Inconel, a nickel–chromium alloy, used in the outer sheath of Thermocoax wires used to heat the substrate heater and the sulfur–evaporation crucible.

4.4 Rutherford Backscattered Spectrometry (RBS) of deposited pyrite thin films

The stoichiometry and thickness of deposited thin films was determined using RBS analysis and RUMP simulations. The average stoichiometric ratio of S:Fe was found to be 2:1 for all deposition temperatures, except at low deposition temperatures of 300°C and 320°C. This suggests that any less strongly bonded sulfur is desorbed during anneals above 325°C. Note that the vapor pressure of sulfur is sufficiently high that we can rule out free sulfur on the surface being the main source of this excess sulfur component.

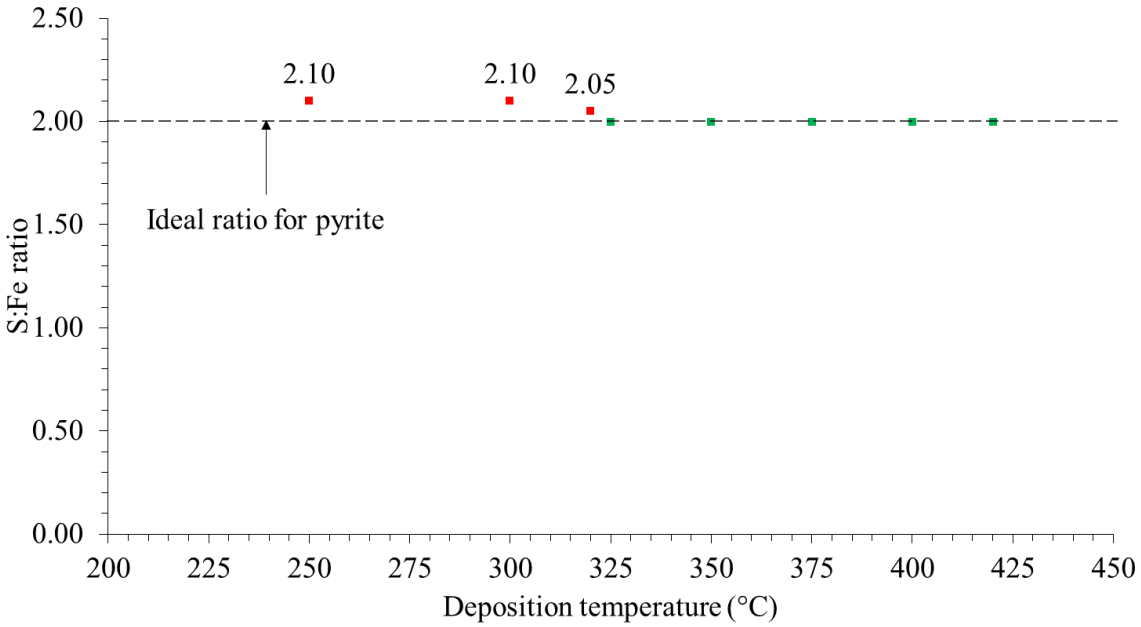

Fig. 12. S:Fe ratio in deposited thin films determined from RBS simulation

4.5 X–ray Diffraction (XRD) of deposited pyrite thin films

I found that increasing the substrate temperature yields better structural quality thin films, as judged by the full–width at half maximum (FHWM) of the pyrite (200) Bragg X–ray diffraction peak.

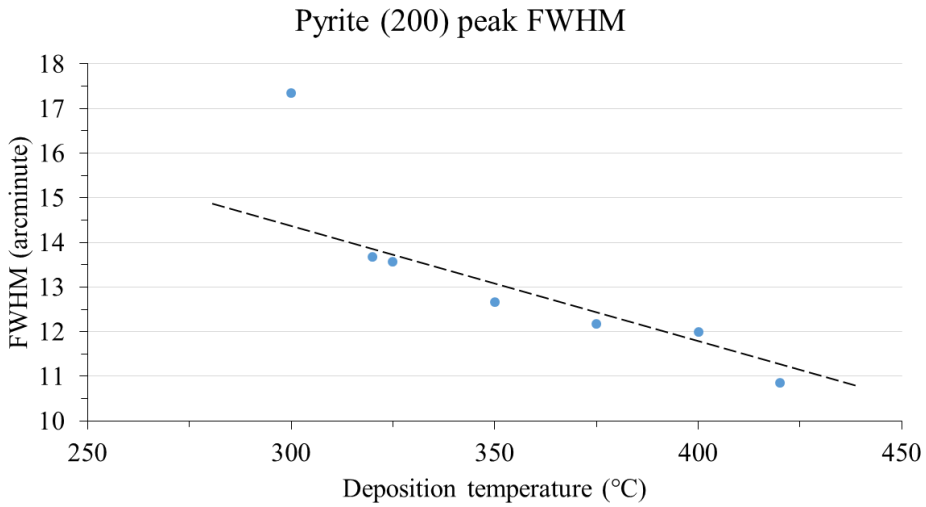

Fig. 13. FWHM of pyrite (200) peak in XRD plots of deposited thin films

4.6 Raman Spectroscopy of deposited pyrite thin films

Pyrite and marcasite are polymorphs of FeS_2 with cubic and orthorhombic structure respectively. Surprisingly, almost all of the Bragg peaks observed in X–ray diffraction of these compounds occur at similar 2θ values. In contrast, the Raman spectra differ significantly. Raman peaks for pyrite occur at frequencies of 343 cm^{-1} (A_g), 379 cm^{-1} (E_g) and 430 cm^{-1} (T_g) while those for marcasite occur at 323 cm^{-1} and 386 cm^{-1} [12]. The Raman spectra which I obtained from Natural Pyrite samples (fig. 9), namely NP–Spain and NP–Utah, contain peaks which are in close agreement with published data.

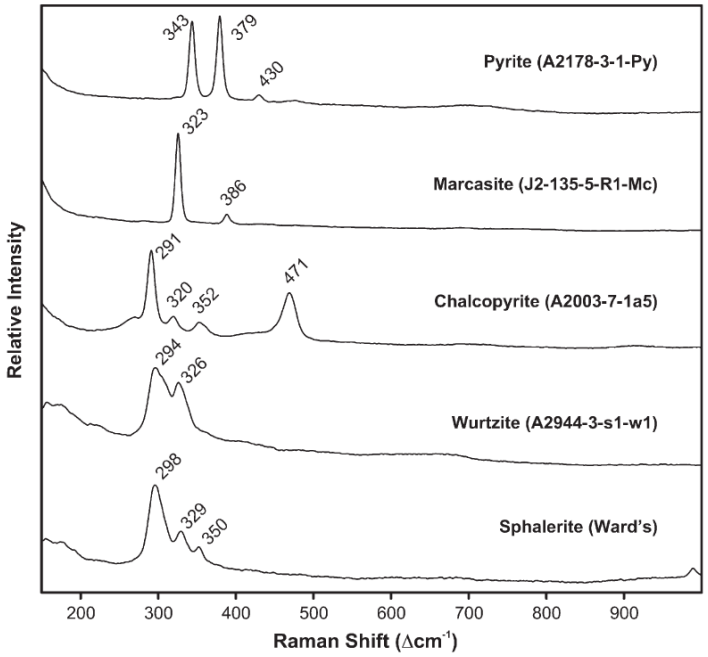

Fig. 14. Raman spectra from iron sulfides obtained using green (523 nm) excitation [12]

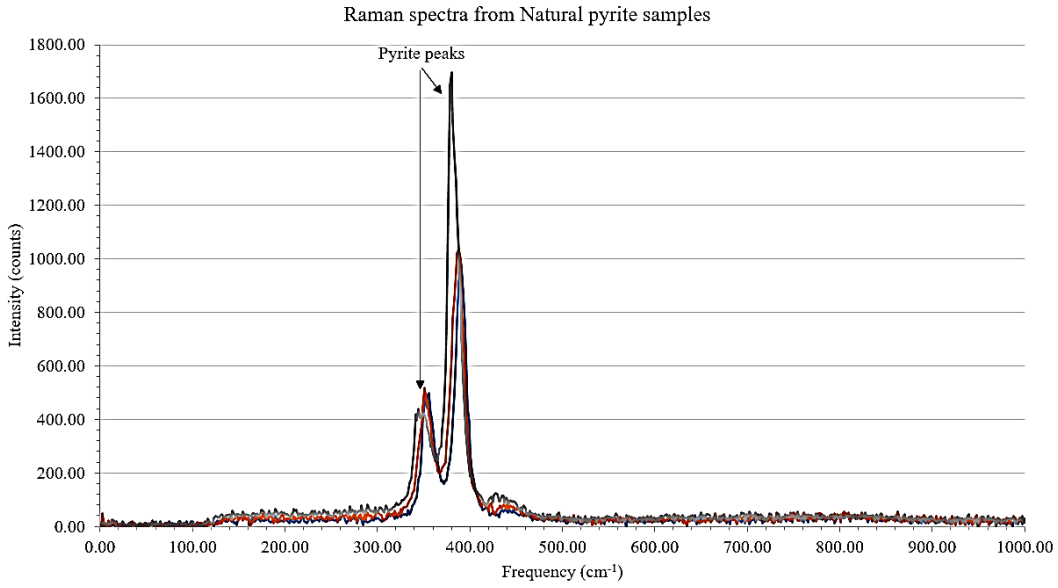

Fig. 15. Raman spectra obtained from natural pyrite samples

(Grey: NP–Spain; Blue and Orange: NP–Utah)

By performing Raman spectroscopy measurements on deposited thin films, I was able to distinguish between pyrite and marcasite thin films. I also quantified the relative

percentage of marcasite phase in pyrite thin films by comparing relative intensities of most dominant Raman peaks. Some Raman spectra from deposited pyrite thin films showed a silicon substrate peak at ~520 cm^{-1}. Raman spectra obtained from films showing Pyrite: Marcasite proportions of 99:1 and 49:51 are shown for visual comparison in fig. 16. In the subsequent figure, the percentage of pyrite in deposited thin films (i.e. pyrite:marcasite ratio) is seen to increase increases with increasing deposition temperature.

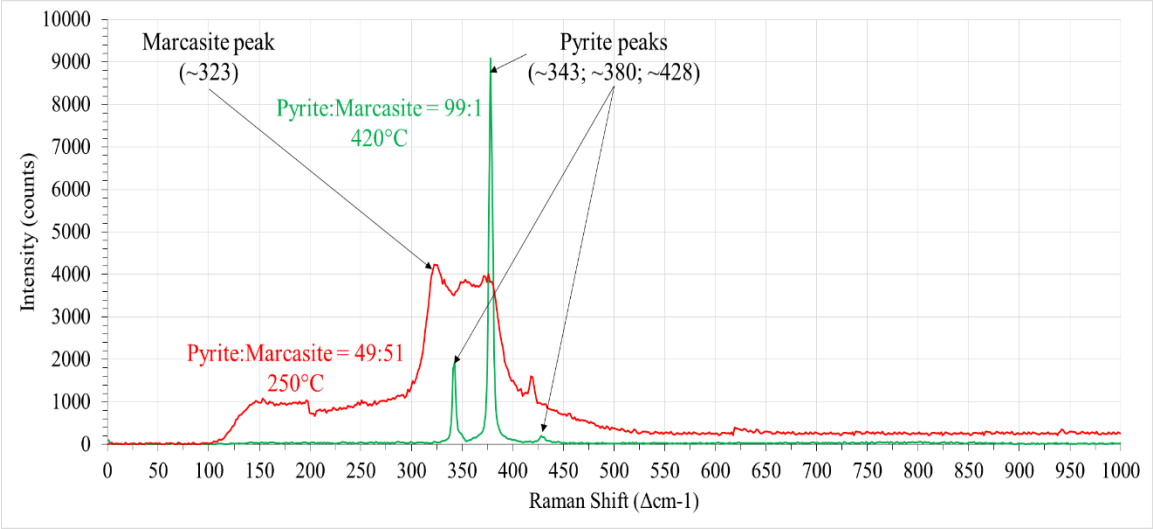

Fig. 16. Raman spectra from films with Pyrite: Marcasite ratios of 99:1 and 49:51

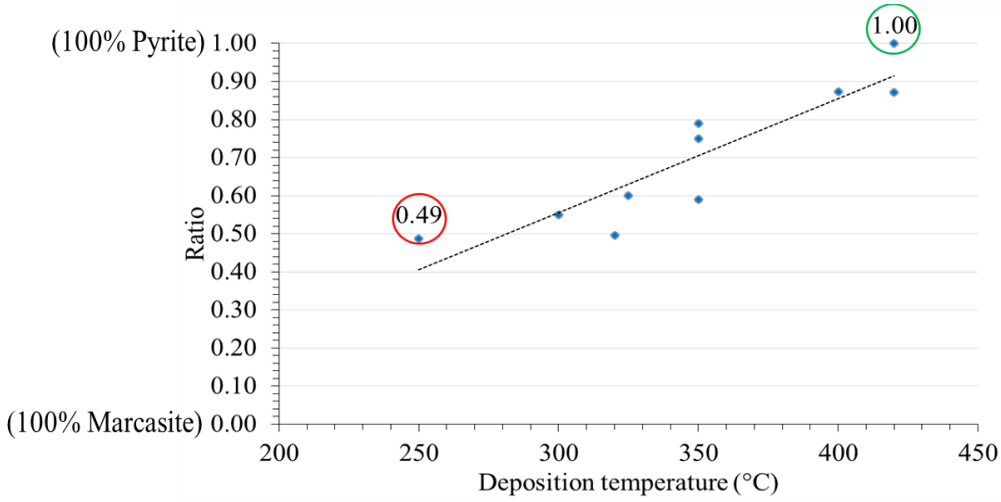

Fig. 17. Plot showing ratio between pyrite and marcasite phases present in deposited films

4.7 Optical topography of deposited pyrite thin films

The optical topography of the pyrite thin films deposited in the upgraded chamber was characterized using an optical profilometer (Zemetrics, Model ZeScope, at LeRoy Eyring Center for Solid State Science) with a depth resolution better than 1 Å. The figure below shows that the average roughness decreases with increasing deposition temperature. This can be attributed to improved diffusion and mass transport at elevated temperatures on the growth surface.

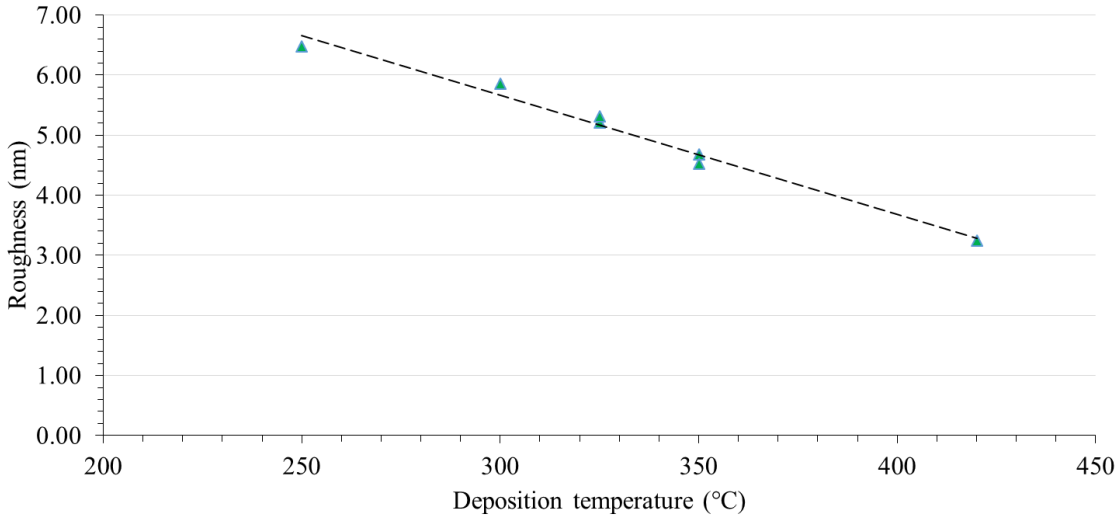

Fig. 18. Plot showing relation between optical roughness of deposited thin films and deposition temperature

4.8 UV/Vis/Near–IR spectroscopy of deposited pyrite thin films

Transmission and reflection measurements were performed on pyrite thin films deposited in the upgraded chamber using a spectrophotometer (PerkinElmer, Model Lambda 950 S with Automated Reflectance/Transmittance Analyzer (ARTA) accessory). The range of spectrum analyzed during measurements is 250 nm (4.96 eV) to 2000 nm (0.62 eV). The optics configuration of this tool is shown in the figure below. The substrate

is positioned at an angle of 10° with respect to incident beam. The angle between incident and transmitted beam is 180°, while that between incident beam and reflected beam is 20°.

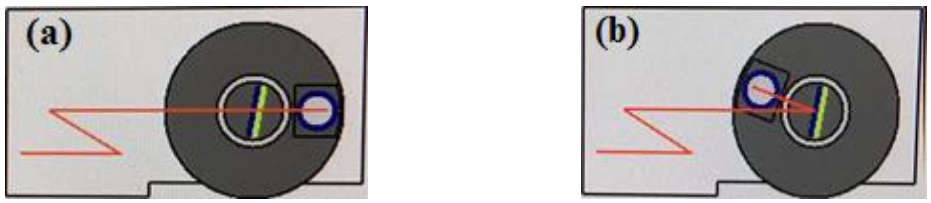

Fig. 19. Schematic diagrams showing optics arrangement in (a) transmission mode; (b) reflection mode

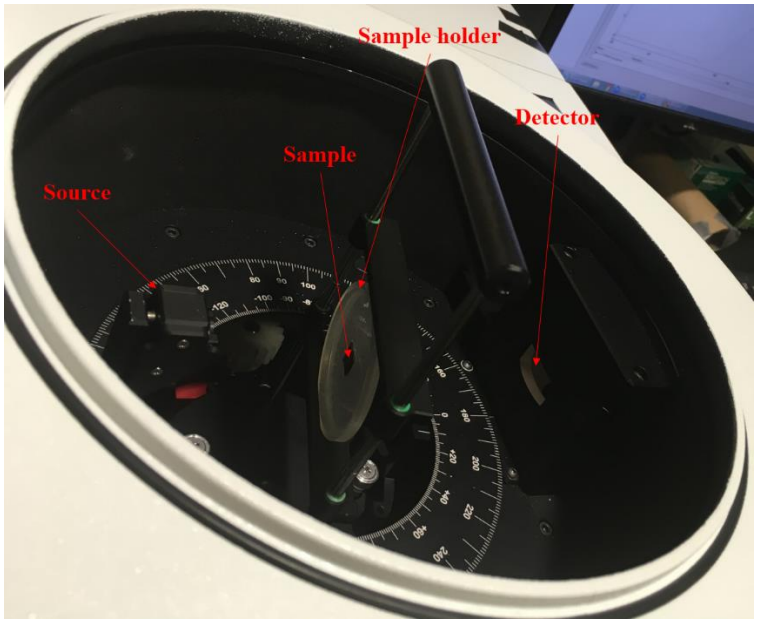

Fig. 20. Arrangement of optics in ARTA accessory during transmission measurements

The pyrite bandgap based on optical measurements has been reported to be 0.9 eV [10]. Fig. 11 shows the reflectivity data measured from pyrite thin films deposited in the upgraded chamber. The peak around 1.5 eV is attributed to 3d intraband transitions from 3d t_{2g} into the antibonding e_g^* state and the second peak at ~ 4.0 eV has been attributed to interband transitions from S 3p band into the Fe 3d e_g^* state [11]. The discontinuity in data points at ~1.48 eV in all the plots is due to an instrumental change in detector optics at this

energy. Using a Tauc plot (i.e. by plotting α^2 versus photon energy), a bandgap energy of 0.94 eV was found in the higher–quality films which were grown at higher temperatures and had the smallest below–bandgap absorption. This value is in close agreement with the reported values in literature [10].

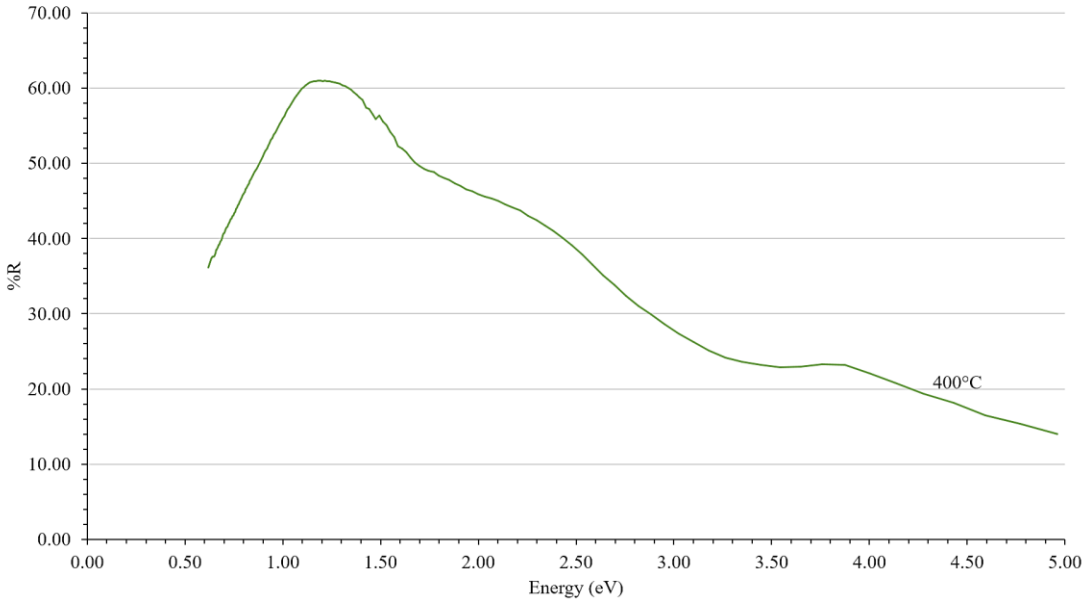

Fig. 21. Reflectivity plot obtained from deposited pyrite thin films

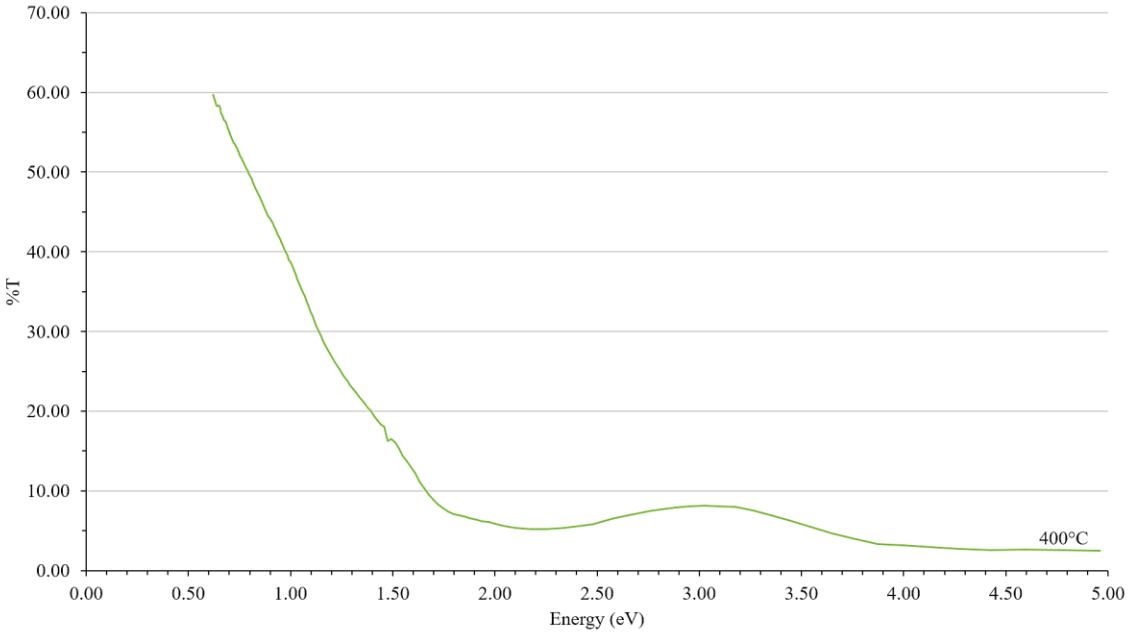

Fig. 22. Transmission data obtained from deposited pyrite thin films

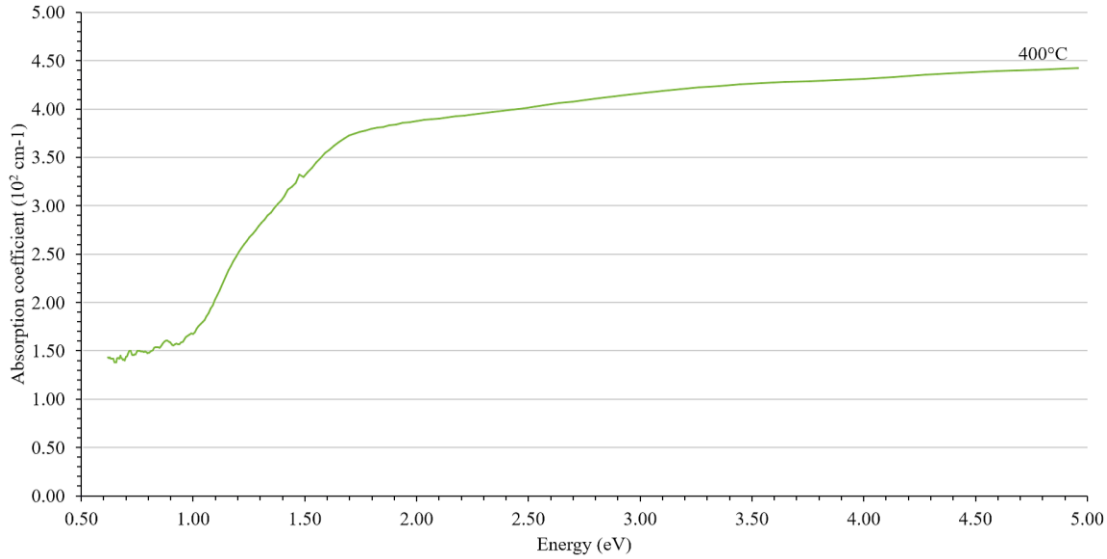

Fig. 23. Variation in absorption coefficient with increasing photon energy

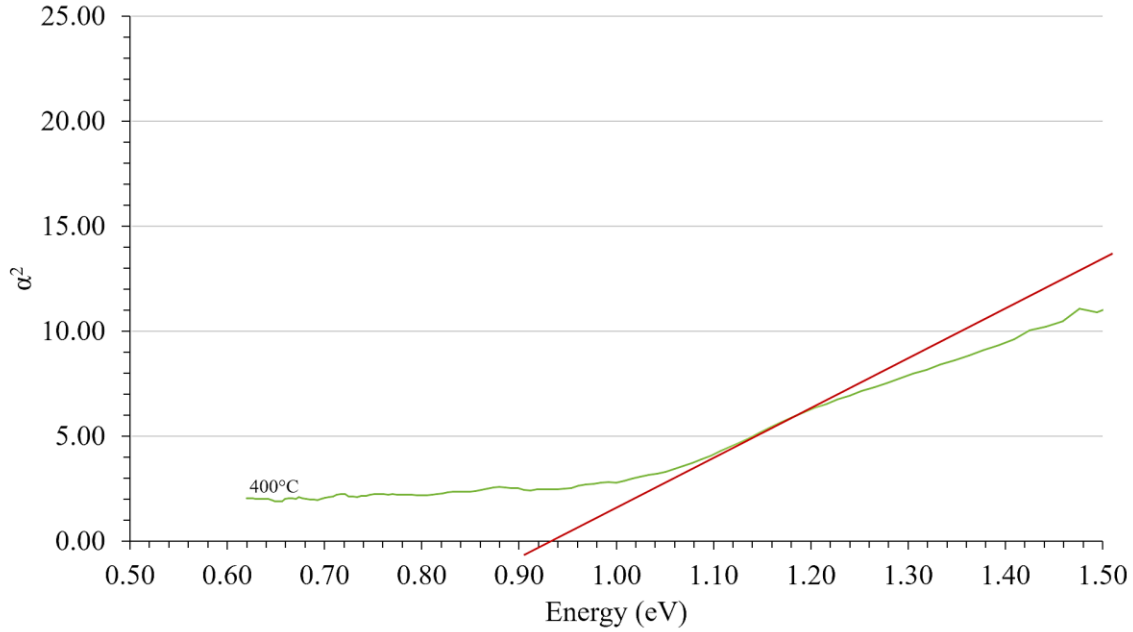

Fig. 24. Estimation of bandgap energy of pyrite thin films using optical method

CHAPTER 5

CONCLUSIONS

Using a systematic material selection process, I designed, built and used a sequential–evaporation growth system to improve the structural quality, surface smoothness, chemical stoichiometry and phase purity of pyrite thin films.

Stoichiometric pyrite thin films were obtained at all temperatures above 325°C. The smoothness of films, as measured by optical profilometer, and crystal quality, as judged by FWHM of X–ray diffraction pyrite (200) Bragg peak, improved with increasing deposition temperature up to highest temperature used, i.e. 420°C. The percentage of pyrite phase in the deposited thin films, as determined from Raman spectra, also increased with increasing deposition temperature up to a value of 100% at 420°C. SIMS measurements from thin films deposited in the upgraded chamber, with mostly Al parts, have contamination levels 3 orders of magnitude smaller than those found for the older chamber, with mostly stainless steel and copper parts. Contamination from some elements such as bromine (Br), lead (Pb) and molybdenum (Mo) has been completely eliminated.

Using a Tauc plot, I measured the bandgap energy of highest–quality pyrite thin films deposited using my chamber to be 0.94 eV.

CHAPTER 6

FUTURE WORK

In order to further reduce impurity concentrations in the deposited pyrite thin films, it is necessary to identify the source of the remaining contaminants. For example, nickel (Ni) is present in the Inconel alloy covering the Thermocoax heating elements. Alternative materials should be sought in order to completely eliminate sources of nickel contamination. An iron heating element might also be considered. A ceramic covering should also be used to cover the wiring, especially where the element enters the heater, since they are not thermally anchored and are thus at a much higher temperature than the rest of the wiring. A thorough study to determine the mean time to failure should be performed.

It was noted that crystal quality and phase purity of pyrite thin films improves with increasing deposition temperature. In order to attain higher deposition temperatures, up to 530°C for 1 Torr sulfur pressure, I would suggest that the aluminum bottom–plate and bottom–disc should be replaced with more heat–resistant materials, like Macor ceramics. Having optimized the chamber for high–structural quality pyrite thin film deposition, doping with donors dopants and acceptor dopants to form n– and p–type pyrite, respectively, can be considered as the next objective. The upgraded chamber built during this project is capable of incorporating an additional evaporation source on the bottom flange.

CHAPTER 7

REFERENCES

1. W. Shockley and H. J. Queisser, "Detailed Balance Limit of Efficiency of p–n Junction Solar Cells", *Journal of Applied Physics* **32** (1960): pp. 510–519

2. Martin A. Green, Keith Emery, Yoshihiro Hishikawa, Wilhelm Warta and Ewan D. Dunlop, "Solar cell efficiency tables (Version 45)", *Progress in Photovoltaics: Research and Applications* **23** (2015): pp. 1–9

3. C. Wadia, A. P. Alivisatos and D. M. Kammen, "Materials Availability Expands the Opportunity for Large–Scale Photovoltaics Deployment", *Environmental Science & Technology* **43** (2009): pp. 2072–2077

4. P. S. Vasekar and T. P. Dhakal, *Thin Film Solar Cells Using Earth–Abundant Materials, Solar Cells – Research and Application Perspectives*, (InTech, 2013, ISBN: 978-953-51-1003-3): pp. 145–168

5. *ASM Handbook* **3**, (ASM International, Ed. Hugh Baker, Materials Park, Ohio, 1992)

6. M. Vahidi, S. W. Lehner, P. R. Buseck and N. Newman, "Growth of epitaxial pyrite (FeS_2) thin films using sequential evaporation", *Acta Materialia* **61** (2013): pp. 7392–7398

7. A. Wertheim, "Growth and Characterization of Pyrite thin films for photovoltaic applications, A thesis submitted in partial fulfillment of the requirements for the degree Masters of Science", (2014): pp. 24–27

8. H. J. T. Ellingham, "Reducibility of Oxides and Sulphides in Metallurgical Processes," Journal of the Society of Chemical Industry **63** (1944): pp. 125–133

9. Y. Alaskar, S. Arafin, Q. Lin, D. Wickramaratne, J. McKay, A. G. Norman, Z. Zhang, L. Yao, F. Ding, J. Zou, M. S. Goorsky, R. K. Lake, M. A. Zurbuchen and K. L. Wang, "Theoretical and experimental study of highly textured GaAs on silicon using a graphene buffer layer", *Journal of Crystal Growth* **425** (2015): p. 271

10. A. Schlegel and P. Wachter, "Optical properties, phonons and electronic structure of iron pyrite (FeS_2)", *Journal of Physics C: Solid State Physics* **9** (1976): pp. 3363–3369

11. I. J. Ferrer, D. M. Nevskaia, C. de las Heras and C. Sánchez, "About the band gap nature of FeS_2 as determined from optical and photo–electrochemical measurements", *Solid State Communications* **74** (1990): pp. 913–916

12. S. N. White, “Laser Raman spectroscopy as a technique for identification of seafloor hydrothermal and cold seep minerals”, *Chemical Geology* **259** (2009): pp. 240–252

13. S. W. Lehner, N. Newman, M. van Schilfgaarde, S. Bandyopadhyay, K. Savage and P. R. Buseck, “Defect energy levels and electronic behavior of Ni–, Co–, and As–doped synthetic pyrite (FeS_2)”, *Journal of Applied Physics* **111** (2012): p. 083717-7